# Electromagnetically driven zonal flows in a rapidly rotating spherical shell

*J. Fluid Mech.* (2013), *vol.* 725, *pp.* 428–445.  
doi:10.1017/jfm.2013.195

# Electromagnetically driven zonal flows in a rapidly rotating spherical shell

**Rainer Hollerbach[1,2,†], Xing Wei[1,3], Jérõme Noir[1] and Andrew Jackson[1]**

[1]Institute of Geophysics, ETH Zürich, Sonneggstrasse 5, 8092 Zürich, Switzerland
[2]Department of Applied Mathematics, University of Leeds, Leeds LS2 9JT, UK
[3]Geophysics Institute, University of Göttingen, D-37077 Göttingen, Germany

(Received 27 June 2012; revised 5 February 2013; accepted 10 April 2013;
first published online 14 May 2013)

We consider the flow of an electrically conducting fluid confined in a rotating spherical shell. The flow is driven by a directly imposed electromagnetic body force, created by the combination of an electric current flowing from the inner sphere to a ring-shaped electrode around the equator of the outer sphere and a separately imposed predominantly axial magnetic field. We begin by numerically computing the axisymmetric basic states, which consist of a strong zonal flow. We next compute the linear onset of non-axisymmetric instabilities, and fully three-dimensional solutions up to ten times supercritical. We demonstrate that an experimental liquid-sodium device 50 cm in diameter could achieve and exceed these parameter values.

**Key words:** free shear layers, high-Hartmann-number flows, MHD and electrohydrodynamics

## 1. Introduction

The Earth's magnetic field is created by convectively driven flows in its rapidly rotating molten-iron outer core (e.g. Jones 2011). There is therefore great interest in studying magnetohydrodynamic flows in rotating systems not only theoretically, but experimentally as well. Convectively driving a flow sufficiently hard to yield a laboratory dynamo is unfortunately not possible, but a number of mechanically driven flows have achieved dynamo action (see for example the reviews by Stefani, Gailitis & Gerbeth 2008; Verhille *et al.* 2010; Lathrop & Forest 2011).

Even these dynamos require very strong forcing, so magnetohydrodynamic effects are often introduced by an externally imposed magnetic field, rather than hoping for a purely internally generated dynamo field. Ensuring that magnetic fields are present at the outset not only reduces the experimental size and power requirements by an order of magnitude, but also yields interesting magnetohydrodynamic phenomena even in the laminar regime, where theoretical predictions and comparisons can more easily be made. In contrast, laboratory dynamos are inevitably turbulent from the outset, making theoretical analysis more difficult.

One imposed-field configuration that has attracted increasing attention is magnetic spherical Couette flow (Hollerbach 1994), in which a flow is driven by differentially

† Email address for correspondence: rh@maths.leeds.ac.uk

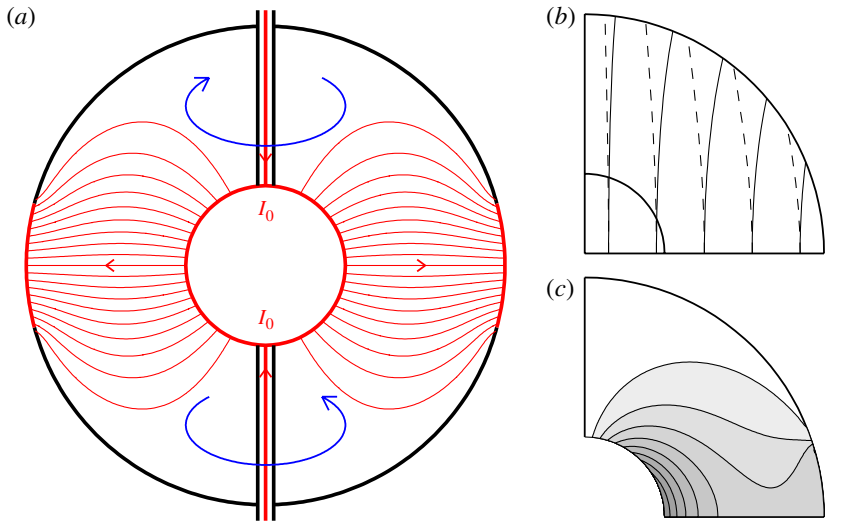


FIGURE 1. (*a*) The basic configuration, consisting of a spherical shell designed so that electric currents can be injected at the inner sphere and extracted at a ring-shaped electrode around the equator of the outer sphere. Black represents insulating parts of the container, red conducting. The red lines within the interior indicate the electrostatic current distribution $\boldsymbol{J}$, before the currents induced by the fluid flow are included. The blue lines denote the associated magnetic field $\boldsymbol{B}_t$. (*b*) Field-lines of the imposed field $\boldsymbol{B}_p$, for $\epsilon = -0.2$ (solid) and $\epsilon = 0.2$ (dashed). (*c*) The Lorentz torque $\boldsymbol{J} \times \boldsymbol{B}_p = -f(r, \theta)\hat{\boldsymbol{e}}_\phi$ (with $\epsilon = 0$ in this case). The contour interval is 1 (non-dimensionalized as in § 2), with the grey-shading indicating increasingly large values. The quantities shown in (*b,c*) are both equatorially and axially symmetric, like $\boldsymbol{J}$ in (*a*).

rotating a spherical shell. Experiments have been performed with imposed axial (Sisan *et al.* 2004; Kelley *et al.* 2007) and dipolar (Nataf *et al.* 2006, 2008; Brito *et al.* 2011) fields. Related theoretical work includes Hollerbach (2009), Soward & Dormy (2010) and Gissinger, Ji & Goodman (2011) and further references therein.

In this work we suggest the possibility of driving a flow electromagnetically rather than mechanically. Specifically, suppose we not only impose magnetic fields $\boldsymbol{B}$, but also inject electric currents $\boldsymbol{J}$ into the fluid. The resulting Lorentz force $\boldsymbol{J} \times \boldsymbol{B}$ will then directly drive a flow, without the need for any differential rotation or other mechanical forcing. Experiments involving electromagnetically driven flows of this type have been carried out before (e.g. Messadek & Moreau 2002; Moresco & Alboussière 2004; Rossi, Vassilicos & Hardalupas 2006; Figueroa *et al.* 2009; Boisson *et al.* 2012; Seilmayer *et al.* 2012), but not with geodynamo applications in mind. The novel aspect of our approach here is to drive such flows in a rapidly rotating spherical shell, in order to model aspects of the Earth's core.

Figure 1(*a*) illustrates the geometry and current injection that we envisage. We start with a spherical shell, with radius ratio $r_i/r_o = 1/3$, chosen to be comparable with the Earth's inner/outer core radius ratio of 0.35. The entire system is in solid-body rotation, but there is no differential rotation of the inner and outer spheres. The shafts suspending the inner sphere are designed such that electric currents $2I_0$ can be injected into the inner sphere, which is made of a conducting material such as copper. From this inner-sphere electrode the currents flow through the fluid (liquid sodium) to a ring-shaped electrode that extends $\pm 15^\circ$ from the equator of the outer sphere. (The

current injection along the top and bottom shafts, as well as the return flows from the outer electrode to close the current loops are kept as symmetric as possible, to preserve the system's equatorial symmetry.)

Associated with this distribution of electric currents is an azimuthal magnetic field $\boldsymbol{B}_t$ (the subscript $t$ refers to toroidal), satisfying $\nabla \times \boldsymbol{B}_t = \mu \boldsymbol{J}$, where $\mu$ is the permeability of free space and $\boldsymbol{J}$ the electric current density within the fluid. The specific flow of current shown in figure 1(*a*) is the electrostatic distribution before any fluid flows and electric currents induced thereby are included. Formally, this electrostatic current density $\boldsymbol{J}$ is given by the solution of $\nabla^2 \boldsymbol{B}_t = \boldsymbol{0}$, subject to the $2I_0$ inhomogeneous injection/extraction boundary conditions on $\boldsymbol{J}$, that is, $J_r = 2I_0/4\pi r_i^2$ on the inner boundary, $J_r = 0$ on the insulating parts of the outer boundary, and $J_r = 2I_0/A_r$ on the conducting ring (where $A_r$ denotes the ring's surface area).

Given this imposed electric current density $\boldsymbol{J}$ and its associated magnetic field $\boldsymbol{B}_t$, the resulting Lorentz force $\boldsymbol{J} \times \boldsymbol{B}_t$ is already sufficient to drive a fluid flow $\boldsymbol{U}$. We will nevertheless impose an additional, predominantly axial magnetic field $\boldsymbol{B}_p$ (the subscript $p$ refers to poloidal). We will be interested in the limit where $\boldsymbol{B}_p \gg \boldsymbol{B}_t$, and the Lorentz force $\boldsymbol{J} \times \boldsymbol{B}_t$ is negligible compared with $\boldsymbol{J} \times \boldsymbol{B}_p$. There are several reasons for preferring to drive the system primarily by the imposed force $\boldsymbol{J} \times \boldsymbol{B}_p$ rather than $\boldsymbol{J} \times \boldsymbol{B}_t$.

First, $\boldsymbol{B}_p \gg \boldsymbol{B}_t$ is experimentally quite straightforward to achieve (we will insert specific numbers later on), so if one is interested in forcing the system as hard as possible, it makes sense to impose this additional field $\boldsymbol{B}_p$. Second, the orientations of $\boldsymbol{J}$, $\boldsymbol{B}_t$ and $\boldsymbol{B}_p$ are such that $\boldsymbol{J} \times \boldsymbol{B}_t$ has only $r$- and $\theta$-components, whereas $\boldsymbol{J} \times \boldsymbol{B}_p$ has only a $\phi$-component, where $(r, \theta, \phi)$ are spherical coordinates. The well-known result (e.g. Jones 2011) that in rapidly rotating systems zonal flows are far easier to excite than meridional flows then applies, and indicates that even if $\boldsymbol{J} \times \boldsymbol{B}_p$ only had the same magnitude as $\boldsymbol{J} \times \boldsymbol{B}_t$, it would nevertheless drive a far stronger flow.

A third reason for preferring $\boldsymbol{B}_p$ to $\boldsymbol{B}_t$ is that, owing to the currents $I_0$ along the shafts, $\boldsymbol{B}_t$ near the shafts scales as $s^{-1}$, where $s$ is the cylindrical distance from the axis. Since $s = 0$ would not be part of the fluid domain there is no actual singularity involved, but it would nevertheless be preferable to design an experiment where the precise thickness of the shafts plays less of a role than it might if $\boldsymbol{B}_t$ were the dominant magnetic field. We will see below that $\boldsymbol{B}_t \ll \boldsymbol{B}_p$ is satisfied even near the shafts for all plausible experimental setups. (In the mathematical model considered here though, where there are no shafts, and $s = 0$ is thus included, the neglect of $\boldsymbol{B}_t$ is formally not justified.)

Regarding the specific form of $\boldsymbol{B}_p$, we will take

$$\boldsymbol{B}_p = B_0[\hat{\boldsymbol{e}}_z + \epsilon((2z^2 - s^2)\hat{\boldsymbol{e}}_z - 2sz\hat{\boldsymbol{e}}_s)], \tag{1.1}$$

where $(z, s, \phi)$ are cylindrical coordinates. Figure 1(*b*) shows the resulting field-lines for $\epsilon = \pm 0.2$. There are two reasons for considering not just a purely axial field $\boldsymbol{B}_p = B_0\hat{\boldsymbol{e}}_z$, but non-zero $\epsilon$ as well. First, a purely axial field is somewhat degenerate, in the sense that it is only for a purely axial field that the Taylor–Proudman theorem, tending to align the flow parallel to the axis of rotation, and the Ferraro iso-rotation law, tending to align it along the field, are in complete agreement. For any other imposed field they are at least partially in conflict, and it is of interest to see how the system resolves this conflict. The second reason for considering non-zero $\epsilon$ is that slightly curved fields would be easier to generate in an experiment, requiring only a small number of Helmholtz coils rather than the large array of coils, in either a long cylindrical or spherical-shell configuration (Everett & Osemeikhian 1966), that would

be needed to obtain a purely axial field. The $\epsilon$-part of $\boldsymbol{B}_p$ is then simply the next term in a multi-pole expansion of general potential fields.

Finally, given $\boldsymbol{J}$ and $\boldsymbol{B}_p$, figure 1(*c*) shows the resulting Lorentz force $\boldsymbol{J} \times \boldsymbol{B}_p = -f(r,\theta)\hat{\boldsymbol{e}}_\phi$ that ultimately drives the entire system. In the remainder of this paper we will derive the governing equations, compare them with the magnetic spherical Couette flow and geodynamo equations, and compute solutions forced up to 10 times beyond the onset of non-axisymmetric instabilities. We demonstrate that these parameter values could be obtained experimentally, and estimate how much more strongly the system could be forced.

## 2. Equations

Since the relevant equations, and certain approximations we wish to make, have not been presented before, we will consider them in some detail here. We begin by letting the total magnetic field be given by

$$\boldsymbol{B} = B_0 \boldsymbol{B}_p + \frac{I_0 \mu}{2\pi r_o}(\boldsymbol{B}_t + \boldsymbol{b}), \tag{2.1}$$

where $\boldsymbol{B}_p$ and $\boldsymbol{B}_t$ are the non-dimensional equivalents of the fields introduced above, each appropriately scaled by its own amplitude. The new quantity $\boldsymbol{b}$ is the field induced by the fluid flow $\boldsymbol{U}$; by scaling it in the same way as $\boldsymbol{B}_t$ we are implicitly assuming that the induced currents $\boldsymbol{j} = \boldsymbol{\nabla} \times \boldsymbol{b}$ are comparable to the imposed current $\boldsymbol{J} = \boldsymbol{\nabla} \times \boldsymbol{B}_t$.

If we further scale length by the outer-sphere radius $r_o$, time as $r_o^2/\nu$, and $\boldsymbol{U}$ as $\nu/r_o$, where $\nu$ is the fluid viscosity, the non-dimensional Navier–Stokes and induction equations become

$$\frac{\partial \boldsymbol{U}}{\partial t} + \boldsymbol{U} \cdot \boldsymbol{\nabla}\boldsymbol{U} + \tau\, \hat{\boldsymbol{e}}_z \times \boldsymbol{U} = -\boldsymbol{\nabla} p + \nabla^2 \boldsymbol{U} + A[\boldsymbol{\nabla} \times (\boldsymbol{B}_t + \boldsymbol{b})] \times [\boldsymbol{B}_p + \delta(\boldsymbol{B}_t + \boldsymbol{b})], \tag{2.2}$$

$$Pm\,\delta \frac{\partial \boldsymbol{b}}{\partial t} = Pm\, \boldsymbol{\nabla} \times \left(\boldsymbol{U} \times \left[\boldsymbol{B}_p + \delta(\boldsymbol{B}_t + \boldsymbol{b})\right]\right) + \delta\, \nabla^2 \boldsymbol{b}. \tag{2.3}$$

The parameter

$$A = \frac{I_0 B_0 r_o}{2\pi \rho \nu^2}, \tag{2.4}$$

where $\rho$ is the fluid density, measures the strength of the imposed Lorentz force $\boldsymbol{J} \times \boldsymbol{B}_p$. The parameter

$$\delta = \frac{I_0 \mu}{2\pi r_o B_0} \tag{2.5}$$

represents the ratio of $\boldsymbol{B}_t$ to $\boldsymbol{B}_p$; following our discussion above we will therefore be interested in the limit $\delta \ll 1$. The Coriolis number

$$\tau = \frac{2\Omega r_o^2}{\nu} \tag{2.6}$$

measures the solid-body rotation $\Omega$ of the entire system. Finally, the magnetic Prandtl number

$$Pm = \frac{\nu}{\eta} \tag{2.7}$$

is the ratio of the fluid viscosity $\nu$ to magnetic diffusivity $\eta$, and is thus a material property of the fluid. The value for liquid sodium is $7.5 \times 10^{-6}$ (e.g. Brito *et al.* 2011). In deriving these equations we have also used the fact that $\boldsymbol{B}_p$ and $\boldsymbol{B}_t$ satisfy $\boldsymbol{\nabla} \times \boldsymbol{B}_p = \boldsymbol{0}$ and $\nabla^2 \boldsymbol{B}_t = \boldsymbol{0}$, and are steady; all dynamic variations in $\boldsymbol{B}$ are accounted for by the induced field $\boldsymbol{b}$.

Up to this point these equations are exact. We now use $\delta \ll 1$ and $Pm \ll 1$ to approximate them as

$$\frac{\partial \boldsymbol{U}}{\partial t} + \boldsymbol{U} \cdot \boldsymbol{\nabla} U + \tau\, \hat{\boldsymbol{e}}_z \times \boldsymbol{U} = -\boldsymbol{\nabla} p + \nabla^2 \boldsymbol{U} + A\big[\boldsymbol{\nabla} \times (\boldsymbol{B}_t + \boldsymbol{b})\big] \times \boldsymbol{B}_p, \tag{2.8}$$

$$\boldsymbol{0} = Pm\, \boldsymbol{\nabla} \times (\boldsymbol{U} \times \boldsymbol{B}_p) + \delta \nabla^2 \boldsymbol{b}, \tag{2.9}$$

analogous to the $Rm \ll 1$ approximation made in many numerical studies of magnetic spherical Couette flow (e.g. Hollerbach 2009). Physically, these simplified equations correspond to stating that: (*a*) the magnetic field is essentially just $\boldsymbol{B}_p$, and does not change, (*b*) the electric currents consist of both the externally imposed $\boldsymbol{J} = \boldsymbol{\nabla} \times \boldsymbol{B}_t$ and the induced $\boldsymbol{j} = \boldsymbol{\nabla} \times \boldsymbol{b}$, and (*c*) $\boldsymbol{b}$ is induced by the action of $\boldsymbol{U}$ on $\boldsymbol{B}_p$, and adjusts effectively instantaneously.

It is convenient to further rescale $\boldsymbol{U}$ and $\boldsymbol{b}$ according to

$$\boldsymbol{U} = \frac{A}{\tau} \hat{\boldsymbol{U}}, \quad \boldsymbol{b} = \frac{Pm}{\delta} \frac{A}{\tau} \hat{\boldsymbol{b}}. \tag{2.10}$$

Recalling also that $(\boldsymbol{\nabla} \times \boldsymbol{B}_t) \times \boldsymbol{B}_p = -f(r,\theta) \hat{\boldsymbol{e}}_\phi$ is the known forcing term that ultimately drives everything, the final result is

$$E \frac{\partial \hat{\boldsymbol{U}}}{\partial t} + E\hat{A}\, \hat{\boldsymbol{U}} \cdot \boldsymbol{\nabla} \hat{U} + \hat{\boldsymbol{e}}_z \times \hat{\boldsymbol{U}} = -\boldsymbol{\nabla} \hat{p} + E\, \nabla^2 \hat{\boldsymbol{U}} + \Lambda\, (\boldsymbol{\nabla} \times \hat{\boldsymbol{b}}) \times \boldsymbol{B}_p - f(r,\theta) \hat{\boldsymbol{e}}_\phi, \tag{2.11}$$

$$\boldsymbol{0} = \boldsymbol{\nabla} \times (\hat{\boldsymbol{U}} \times \boldsymbol{B}_p) + \nabla^2 \hat{\boldsymbol{b}}. \tag{2.12}$$

The three non-dimensional parameters are now the Ekman and Elsasser numbers

$$E = \tau^{-1} = \frac{\nu}{2\Omega r_o^2}, \quad \Lambda = \frac{Pm}{\delta} \frac{A}{\tau} = \frac{B_0^2}{2\Omega \mu \rho \eta}, \tag{2.13}$$

and the forcing parameter

$$\hat{A} = \frac{A}{\tau} = \frac{I_0 B_0}{4\pi \rho \nu \Omega r_o}. \tag{2.14}$$

The definition of $\hat{A}$ as $A/\tau$ is of course to a certain extent arbitrary; one could equally well have defined it as $A/\tau^2$, in which case the corresponding factor in (2.11) would have been just $\hat{A}$ rather than $E\hat{A}$. There are two reasons why the choice $\hat{A} = A/\tau$ is particularly convenient. First, it matches the rescalings (2.10). Second, as we will see in § 4, the critical values $\hat{A}_c$ for the onset of non-axisymmetric instabilities then exhibit relatively little variation with $E$.

To summarize, the flow $\hat{\boldsymbol{U}}$ evolves in time according to (2.11), and at each instant in time the induced field $\hat{\boldsymbol{b}}$ is determined by (2.12). The boundary conditions associated with (2.11) are no-slip at both boundaries. For the boundary conditions associated with (2.12), we take the inner sphere to be perfectly conducting, meaning that the system has total freedom to rearrange precisely how the injected current enters the fluid. The outer sphere is here taken to be insulating, meaning that the system has no freedom to

rearrange how the current is extracted at the ring-shaped electrode. In reality of course this electrode cannot be insulating, and the system will inevitably have at least some freedom to rearrange precisely where on the electrode the current is extracted. (That is, the boundary conditions on $\boldsymbol{B}_t$ and $\hat{\boldsymbol{b}}$ are formally inconsistent.)

Both the inner and outer boundary conditions are therefore only a plausible approximation of the true conditions, which would inevitably depend on the precise details of how the inner and outer electrodes are manufactured. Varying the conductivity of the inner boundary is easily implemented, with sample calculations indicating that as long as it is greater than that of the fluid, the results are qualitatively like the perfectly conducting results presented here. (For comparison, the conductivity of copper is $\sim$4 times that of liquid sodium.) Implementing more accurate approximations of the outer boundary conditions would be more difficult, and would probably also depend even more sensitively on the specific construction details. However, as long as the latitudinal extent of this equatorial ring is reasonably small, there simply is no space for much rearrangement anyway, so assuming no rearrangement is likely to be a good approximation. (One would not want to make this ring so narrow though that its total surface area was smaller than that of the inner sphere, as otherwise the current densities would become artificially large near the ring.)

These equations (2.11) and (2.12) and associated boundary conditions were solved using the numerical code described by Hollerbach (2000), in which the angular structure is expanded in spherical harmonics, and the radial structure in Chebyshev polynomials. The time stepping of (2.11) is implemented by a second-order Runge–Kutta scheme, modified to treat the diffusive terms implicitly. The highest resolutions used were $(r, \theta) = (200, 300)$ for the two-dimensional calculations in §§ 3 and 4, and $(r, \theta, \phi) = (80, 150, 60)$ for the three-dimensional calculations in § 5.

Comparing these equations with those of magnetic spherical Couette flow, we note that they are very similar, the only real difference being that here the system is driven by the imposed torque $-f(r, \theta)\hat{\boldsymbol{e}}_\phi$ rather than by an imposed differential rotation between the inner and outer spheres. However, electromagnetically driven flows allow greater flexibility, in terms of what body forces to impose, whereas in Couette flows one can only vary the amplitude of the differential rotation, there being no further flexibility in terms of the spatial structure of the forcing.

Finally, comparing with the geodynamo equations, some similarities are that here, too, we will be able to reach the rapidly rotating regime $E \ll 1$ (although inevitably still not as small as in the Earth's core), and also the strongly magnetic regime $\Lambda \geqslant 1$. The main difference is that here the only nonlinear term is $\boldsymbol{U} \cdot \boldsymbol{\nabla} \boldsymbol{U}$ in the Navier–Stokes equation, which is very small in the Earth's core. In contrast, two important nonlinearities in the Earth's core are the total Lorentz force $(\boldsymbol{\nabla} \times \boldsymbol{B}) \times \boldsymbol{B}$ in the Navier–Stokes equation, and the total $\boldsymbol{\nabla} \times (\boldsymbol{U} \times \boldsymbol{B})$ in the induction equation, which are both present only in linearized form in our system here. (Or if one does not make the small-$\delta$ approximation, these nonlinearities are present, but invariably of lesser importance.) Another important factor in the Earth's core is the buoyancy force that ultimately drives the entire geodynamo, whereas in isothermal systems such as considered here buoyancy forces play no role. These differences in the relative importance of the various terms are unfortunately inevitable in laboratory experiments (and are present in spherical Couette flow as well).

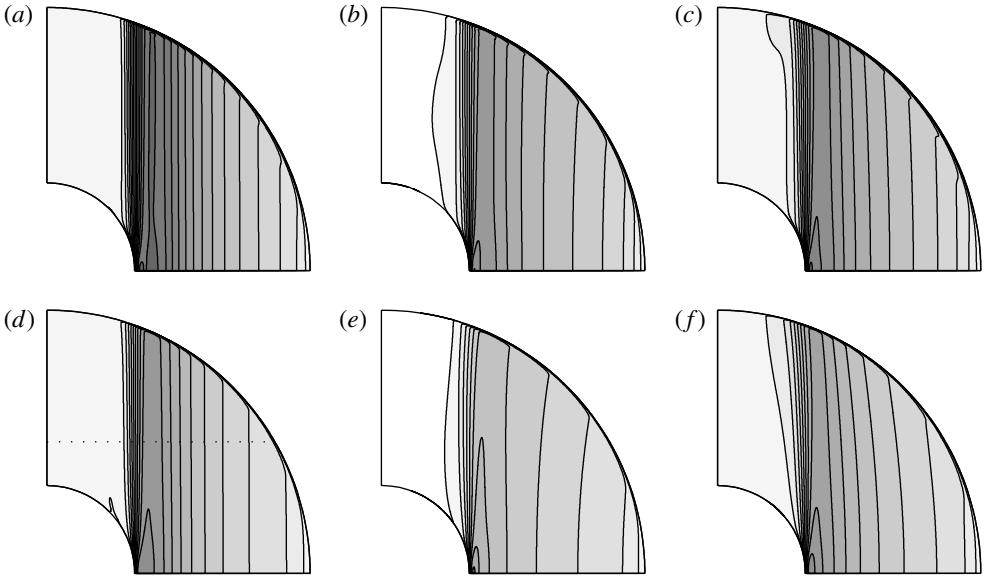


FIGURE 2. Contours of the angular velocity $\hat{\omega} = \hat{U}_\phi/s$, with a contour interval of 100, and the grey-shading indicating increasingly large negative values. $\hat{A} = 0$ and $E = 10^{-5}$; and (*a–c*) $\Lambda = 1$, (*d–f*) $\Lambda = 3$. From left to right $\epsilon = 0$, $-0.2$ and 0.2.

## 3. Axisymmetric basic states

We begin by illustrating the axisymmetric basic states that arise in the case of infinitesimally weak forcing, corresponding to setting $\hat{A} = 0$ in (2.11). Figure 2 shows the angular velocity $\hat{\omega} = \hat{U}_\phi/s$, which is exactly as one might expect; the torque $-f(r,\theta)\hat{\boldsymbol{e}}_\phi$ induces a strong zonal flow also in the $-\hat{\boldsymbol{e}}_\phi$-direction. The second feature to note is how this zonal flow is concentrated almost entirely outside the tangent cylinder, resulting in a shear layer similar to the classical Stewartson (1966) layer. Comparing results at $\Lambda = 1$ and 3, and $\epsilon = 0$ and $\pm 0.2$, we can also see the competing effects of the Taylor–Proudman and Ferraro theorems alluded to earlier: at $\Lambda = 1$ all three values of $\epsilon$ still yield contours that are primarily aligned with the rotation axis, whereas at $\Lambda = 3$ the greater influence of the magnetic field causes the contours to align more with the field-lines of $\boldsymbol{B}_p$.

The dotted line in figure 2(*d*) indicates the line $z = 0.5$. Figure 3 shows profiles of the angular velocity $\hat{\omega}$ along this line, for the purely axial $\epsilon = 0$ field, $E = 10^{-5}$–$10^{-7}$, and $\Lambda = 0.1$, 1 and 3. Also shown is the asymptotic formula (Proudman 1956)

$$\hat{\omega}_g = -\sqrt{2}E^{-1/2}\frac{(1-s^2)^{1/4}}{s}\int_0^{\sqrt{1-s^2}} f(r,\theta)\,\mathrm{d}z \tag{3.1}$$

that comes from balancing the $z$-integrated torque at a given $s$ against the viscous drag in the Ekman boundary layer. We see that for $\Lambda = 0.1$ the agreement is excellent. (Verifying this formula was the main reason for including the otherwise not so interesting $\Lambda = 0.1$ case, which corresponds to a very weak field $\boldsymbol{B}_p$, and hence essentially non-magnetic dynamics.) For $\Lambda = 1$ and 3 the profiles of $\hat{\omega}$ are qualitatively similar, but somewhat suppressed. In terms of the torque balance (3.1), this can be understood by the transition from an initially non-magnetic Ekman layer to a thinner

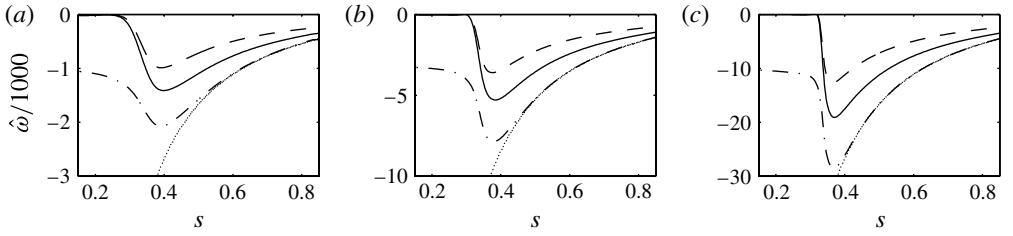


FIGURE 3. Profiles of angular velocity $\hat{\omega}/1000$ as a function of cylindrical radius $s$ along the line $z = 0.5$. $\hat{A} = 0$ and $\epsilon = 0$; and (*a*) $E = 10^{-5}$, (*b*) $10^{-6}$, (*c*) $10^{-7}$. The grey dotted lines show the geostrophic flow formula (3.1), dash-dotted corresponds to $\Lambda = 0.1$, solid to $\Lambda = 1$, and dashed to $\Lambda = 3$.

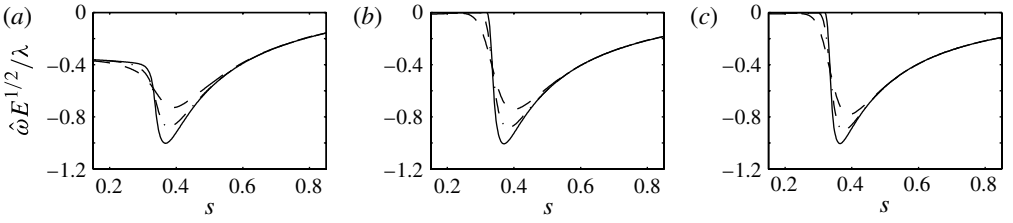


FIGURE 4. The same $\hat{\omega}$ profiles as in figure 3, but now plotted as $\hat{\omega}E^{1/2}/\lambda$, where the proportionality constant $\lambda$ is 9 for $\Lambda = 0.1$ (*a*), 6 for $\Lambda = 1$ (*b*), and 4 for $\Lambda = 3$ (*c*). Dashed lines denote $E = 10^{-5}$, dash-dotted $E = 10^{-6}$, and solid $E = 10^{-7}$. The broad similarity of all nine scaled profiles (at least in the region outside the tangent cylinder at $s = 1/3$) indicates the universal scaling $\hat{\omega} \sim \lambda E^{-1/2}$ (and for $\Lambda \gg 1$ there would most likely even be a simple scaling between $\lambda$ and $\Lambda$).

Ekman–Hartmann layer: among the factors included on the right-hand side of (3.1) is the thickness of the boundary layer, so a thinner layer yields a reduced geostrophic flow.

Figure 4 shows the same profiles as in figure 3, but rearranged to bring out the asymptotic scalings more clearly, and emphasize the underlying similarities. For $\Lambda = O(1)$ we see that $|\hat{\omega}|_{max}$ scales roughly as $5E^{-1/2}$, or $5\hat{A}E^{-1/2}$ for the original unscaled $\omega$. Remembering also how we initially non-dimensionalized $\boldsymbol{U}$, we obtain $Ro \sim 10\hat{A}E^{1/2}$ for the so-called Rossby number, measuring the ratio of the differential rotation $\omega$ to the solid-body rotation $\Omega$. If the forcing is sufficiently strong such that $\hat{A} > E^{-1/2}/10$ – which we will see below is experimentally achievable, e.g. $\hat{A} > 100$ at $E = 10^{-6}$– the Rossby number could thus become $O(1)$. This contrasts with the Earth's core, where $Ro \ll 1$. (These results in figures 3 and 4 were all obtained in the infinitesimal-forcing limit $\hat{A} = 0$, but finite-$\hat{A}$ results are very similar, at least up to the onset of non-axisymmetric instabilities, demonstrating the usefulness of the rescaling (2.10), and the validity of this estimate for $Ro$.)

Figures 3 and 4 show results only for the purely axial field $\epsilon = 0$. Figure 5 shows the corresponding results for $\epsilon = \pm 0.1$ and $\pm 0.2$. An increasingly large $s$-component in $\boldsymbol{B}_p$, of either sign, is seen to suppress $\hat{\omega}$, so much so that $|\hat{\omega}|_{max}$ no longer scales as $E^{-1/2}$ as before. Our previous result for $Ro$ is thus somewhat of an over-estimate for these non-zero-$\epsilon$ cases.

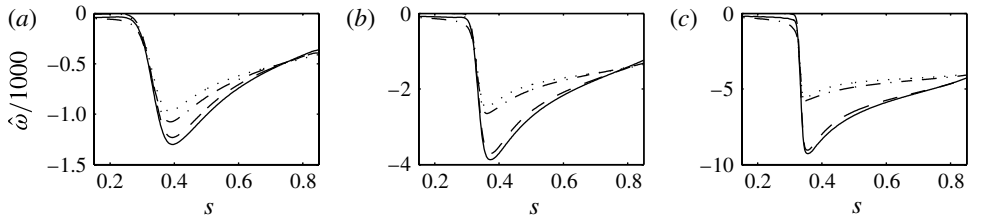


FIGURE 5. As in figure 3, profiles of angular velocity $\hat{\omega}/1000$ as a function of $s$ along the line $z = 0.5$. $\hat{A} = 0$ and $\Lambda = 1$; and (*a*) $E = 10^{-5}$, (*b*) $10^{-6}$, (*c*) $10^{-7}$. Solid lines denote $\epsilon = 0.1$, dashed lines $\epsilon = -0.1$, dash-dotted $\epsilon = 0.2$, and dotted $\epsilon = -0.2$.

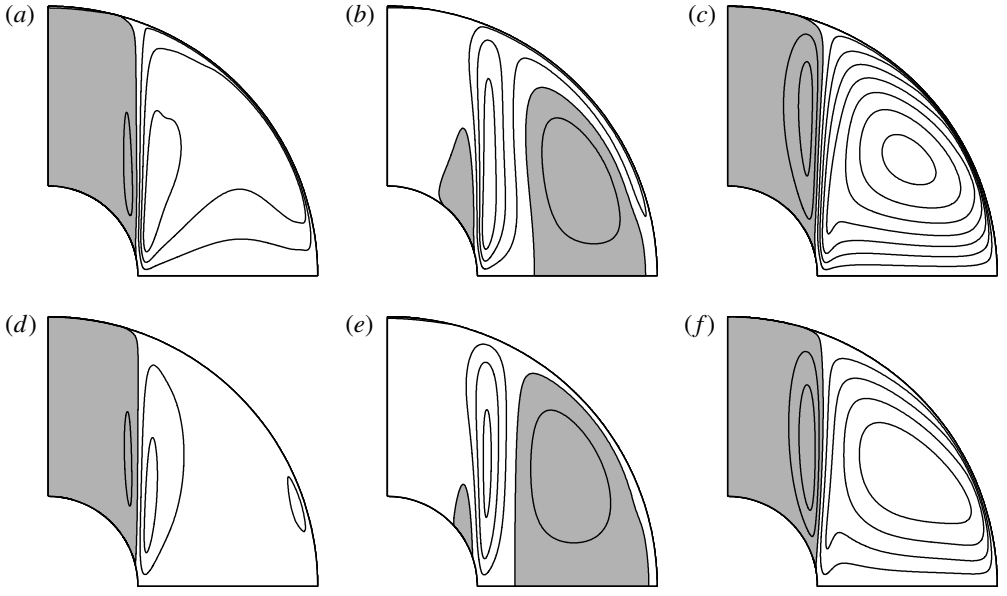


FIGURE 6. Streamlines of the meridional circulation, with white indicating clockwise circulation, grey counter-clockwise, and a contour interval of 0.2. As in figure 2, $\hat{A} = 0$ and $E = 10^{-5}$; and (*a–c*) $\Lambda = 1$, (*d–f*) $\Lambda = 3$, and from left to right $\epsilon = 0$, $-0.2$ and 0.2.

Figures 2–5 have all focused on the basic zonal flow, which is indeed the dominant aspect of the solutions. There is also a weak meridional circulation, shown in figure 6. Unlike $\hat{\omega}$, this circulation does not increase with decreasing $E$, and thus becomes less and less important compared with the zonal flow. (In § 5 we will see that in the sufficiently supercritical regime the solutions do exhibit considerably stronger non-zonal flow components.)

Finally, figure 7 shows how the initial electrostatic current distribution from figure 1(*a*) is altered by the addition of the induced current $\boldsymbol{j} = \boldsymbol{\nabla} \times \boldsymbol{b}$. The net flow is still from the inner sphere to the outer equatorial electrode, as it must be, but some surprisingly complicated patterns emerge, including flows through a very thin Hartmann boundary layer, as well as circulation cells that are closed entirely within the fluid. One other point to note is how the current injection on the inner sphere has

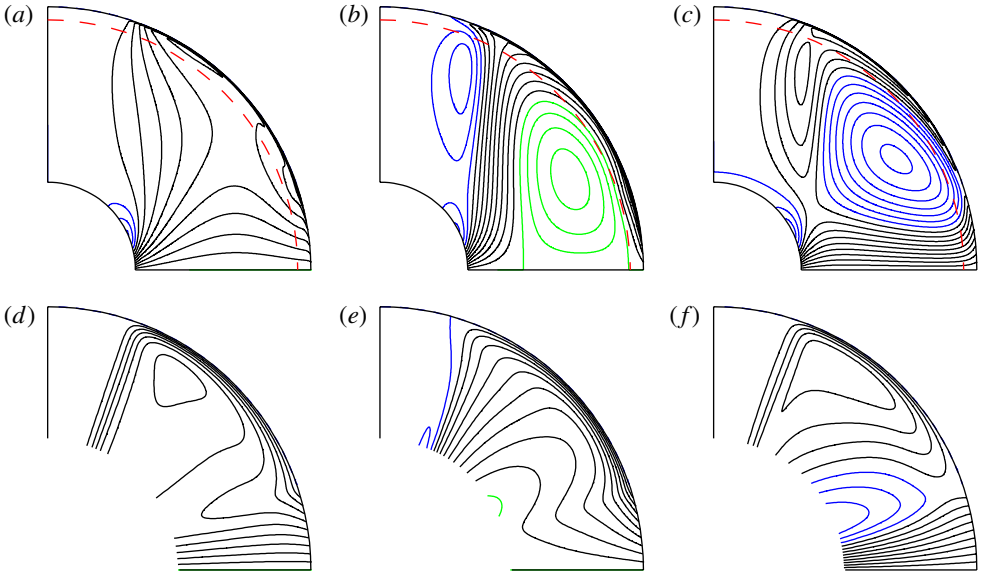


FIGURE 7. (*a–c*) Streamlines of the total electric current distribution. The blue and green contours merely single out certain circulation cells separate from the main current from the inner sphere to the outer equatorial electrode. In (*d–f*) the region between the dashed red lines and the outer boundary in (*a–c*) has been stretched in $r$ by a factor of 10 to properly show the circulation through the outer Hartmann–Ekman boundary layer. $\hat{A} = 0$, $E = 10^{-5}$, $\Lambda = 1$, and from left to right $\epsilon = 0$, $-0.2$ and 0.2, corresponding to figures 2(*a–c*) and 6(*a–c*).

rearranged itself so that essentially all of it enters the fluid at the equator of the inner sphere, rather than uniformly distributed as in figure 1(*a*).

This feature also explains why the angular velocity $\hat{\omega}$ is essentially zero inside the tangent cylinder; there is simply no Lorentz torque driving anything there. One could of course design the inner-sphere electrode to also cover only a portion of the inner sphere, say a small polar cap, thereby forcing electric currents to flow inside the tangent cylinder as well. The result would still be a shear layer on the tangent cylinder: inside the tangent cylinder the formula (3.1) would include a viscous-drag contribution from an inner boundary layer as well, meaning that even a relatively uniform torque would still result in a non-uniform angular velocity (looking similar to the $\Lambda = 0.1$ solutions in figures 3 and 4). The results in this section are therefore broadly representative of what could be achieved with an axisymmetric current flow from an inner electrode to a ring-shaped outer one, independent of the precise details of these electrodes.

## 4. Onset of instabilities

We next computed the forcing that results in the onset of instabilities. As shown in table 1, the critical values $\hat{A}_c$ for the linear onset of non-axisymmetric instabilities are $O(1\text{–}10)$, and vary relatively little with $E$ (and not even monotonically for $\epsilon = \pm 0.2$). Recalling our earlier estimate $Ro \sim 10\hat{A}E^{1/2}$, the corresponding Rossby numbers are thus 0.1–0.01. That is, the onset occurs for (moderately) small $Ro$. Up to onset the

| | $E = 10^{-5}$ | $E = 10^{-6}$ | $E = 10^{-7}$ | $E = 10^{-5}$ | $E = 10^{-6}$ | $E = 10^{-7}$ |
|---|---|---|---|---|---|---|
| $\epsilon = 0$ | 3.4 (5) | 1.8 (10) | 1.2 (19) | −4.5 (6) | −3.0 (11) | −2.1 (22) |
| $\epsilon = 0.1$ | 3.7 (5) | 2.5 (10) | 2.5 (21) | −4.9 (6) | −3.7 (12) | −3.3 (26) |
| $\epsilon = -0.1$ | 4.0 (5) | 2.8 (10) | 2.8 (20) | −4.9 (6) | −3.6 (12) | −3.2 (27) |
| $\epsilon = 0.2$ | 4.9 (5) | 4.3 (11) | 5.3 (23) | −6.3 (6) | −5.5 (13) | −5.7 (27) |
| $\epsilon = -0.2$ | 5.5 (5) | 4.9 (10) | 5.6 (23) | −6.1 (6) | −5.1 (13) | −5.0 (28) |

TABLE 1. Critical positive and negative $\hat{A}$ values for the onset of non-axisymmetric instabilities, having $\phi$-dependence $\exp(im\phi)$, for $E$ and $\epsilon$ as shown, and $\Lambda = 1$ in all cases. The numbers in parentheses indicate the azimuthal wavenumber $m$ of the most unstable modes, which are equatorially symmetric in all cases. A few calculations were also carried out for $\Lambda$ as large as 4, and yielded much the same critical wavenumbers, but with $\hat{A}_c$ around 2–3 times larger.

basic states are also virtually unchanged from the results presented in figures 2 and 7, for example, thereby validating the use of the previous estimate for $Ro$.

We further note in table 1 that there is relatively little difference between positive and negative $\hat{A}$, in terms of either the value $\hat{A}_c$ itself or the associated azimuthal wavenumbers. This is perhaps not surprising, given that instabilities of magnetic Stewartson–Shercliff layers (Wei & Hollerbach 2008) also exhibit less $\pm Ro$ asymmetry than those of non-magnetic Stewartson layers (Hollerbach 2003).

## 5. Three-dimensional solutions

Fully three-dimensional solutions in the supercritical regime are computationally far more demanding than axisymmetric and linear-onset calculations, and were only feasible for $E = 10^{-5}$. Positive and negative $\hat{A}$, and different $\epsilon$, yielded qualitatively similar behaviour. We therefore concentrate on the $\hat{A} > 0$, $\epsilon = 0$ case, and increase $\hat{A}$ as far as possible beyond the linear-onset value $\hat{A}_c = 3.4$.

As indicated in table 1, at onset the solution has azimuthal wavenumber $m = 5$. By the time $\hat{A} = 2\hat{A}_c$, a secondary bifurcation has occurred, whereby the solution switches to an $m = 4$ (and multiples thereof) periodicity in $\phi$. By $3\hat{A}_c$ a further bifurcation has occurred, whereby the solution acquires a (very slight) periodic time-dependence superimposed on the previous steady drift in $\phi$. Similar bifurcations, both the down-shift in $m$ as well as the Hopf bifurcation to a non-trivial time-dependence, have also been observed in magnetic spherical Couette flow (Hollerbach 2009).

Increasing $\hat{A}$ still further, by $5\hat{A}_c$ the $m = 4$ azimuthal periodicity has been lost, and the solution contains energy in all wavenumbers. Unlike the 2 and 3 times supercritical solutions, which remained equatorially symmetric, by $5\hat{A}_c$ the equatorial symmetry has also been lost. Whether the azimuthal and equatorial symmetries are broken in one or two bifurcations is not known; one can construct scenarios consistent with either option. Any hysteresis associated with reducing $\hat{A}$ again was also not investigated in detail. One aspect that was checked though was that if $\hat{A}$ is reduced below $\hat{A}_c$, the solutions inevitably revert back to the original axisymmetric basic states.

The $5\hat{A}_c$ solution also has no simple time-dependence, but fluctuates irregularly. Since it has no further spatial or temporal symmetries to break, it is not surprising that no additional bifurcations occur if $\hat{A}$ is increased further to $10\hat{A}_c$. Figure 8 shows

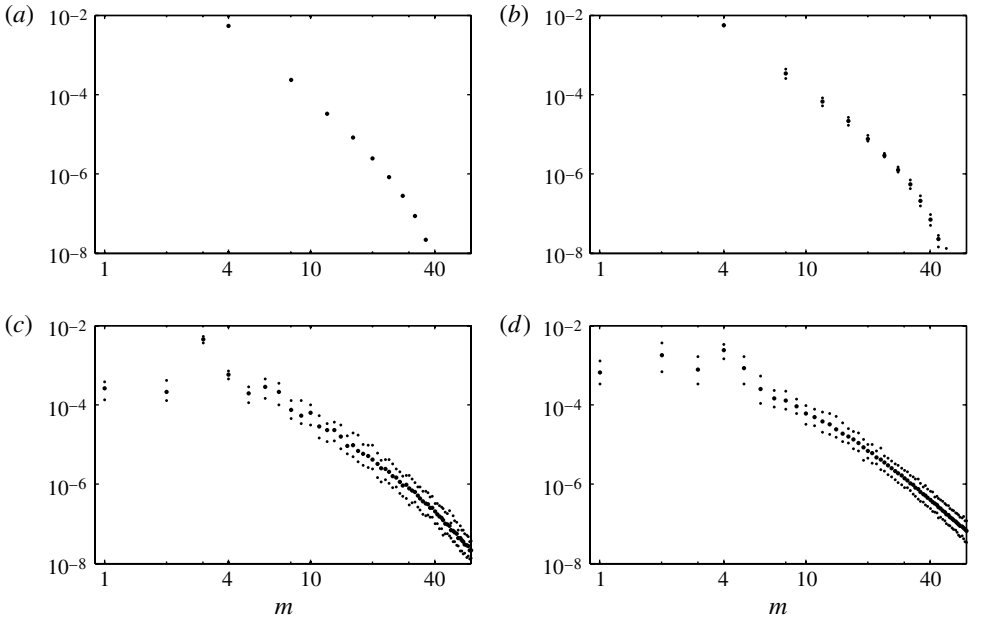


FIGURE 8. Power spectra for (*a*) 2, (*b*) 3, (*c*) 5 and (*d*) 10 times the critical value $\hat{A}_c = 3.4$ corresponding to $E = 10^{-5}$, $\Lambda = 1$ and $\epsilon = 0$, showing the fraction of the total kinetic energy contained in the non-axisymmetric modes $\exp(im\phi)$, for $m = 1$–60. The axisymmetric mode contains ∼99 % of the energy, and is not shown. The spectra in (*a,b*) for 2 and 3 times supercritical include only multiples of $m = 4$. The spectra in (*b–d*) for 3, 5 and 10 times supercritical show both the time-averaged values (larger dots) and the maxima and minima (smaller dots), indicating that the energy in any given $m$ can fluctuate by a factor of up to ∼3.

power spectra for 2, 3, 5 and 10 times $\hat{A}_c$. For 5 and 10 times supercritical the maxima and minima were computed over a time interval of 20 rotations of the system, starting from solutions already equilibrated to a statistically steady state.

For comparison, spinning the basic zonal flow up from rest was found to require $\sim E^{-1/2}/5$ rotations. The factor of $E^{-1/2}$ is the same as in the classical problem where the entire container is spun up from rest (e.g. Duck & Foster 2001), but occurs for a slightly different reason. In the classical problem, it arises from the increasingly inefficient (as $E$ is reduced) role of Ekman pumping in transferring angular momentum into the fluid interior. In contrast, here angular momentum is transferred directly into the interior by the imposed torque $-f(r,\theta)\hat{\boldsymbol{e}}_\phi$. However, the zonal flow that is being spun up itself scales as $E^{-1/2}$ (figure 4), so that a much longer time is also required. Once the zonal flow was spun up there was no evidence of any dynamics occurring on time scales significantly longer than the rotational time scale.

Figures 9 and 10 show snapshots of the detailed spatial structure of the $10\hat{A}_c$ flow. In figure 9 we see a significant broadening of the previous shear layer, as well as an increased $z$-dependence of the zonal flow, with the peak occurring in the equatorial region. We note furthermore how substantially the equatorial symmetry has been broken (in both figures), with only the basic zonal flow still dominated by its equatorially symmetric component. The differences between the two hemispheres also give a good indication of the typical variation in time; the basic zonal flow is always present, with irregular non-axisymmetric fluctuations about it. It is of interest finally

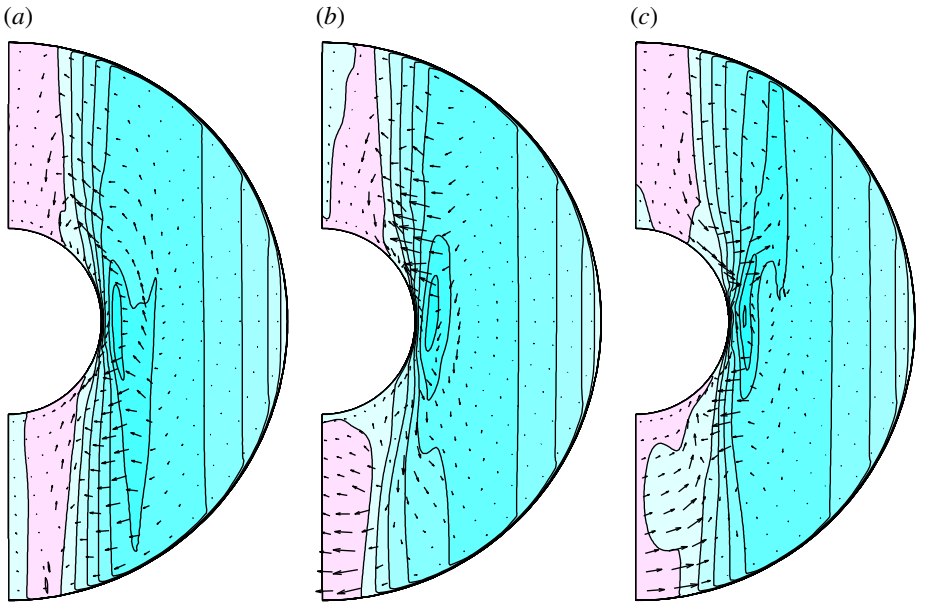


FIGURE 9. Three meridional sections of the $10\hat{A}_c$ flow, each separated by 120°. The contours show $\hat{U}_\phi$, with blue negative, pink positive, and contour interval 100 ($|\hat{U}_\phi|_{max} = 714$). The arrows denote the flow ($\hat{U}_s$, $\hat{U}_z$) in the plane, with a maximum value of 145.

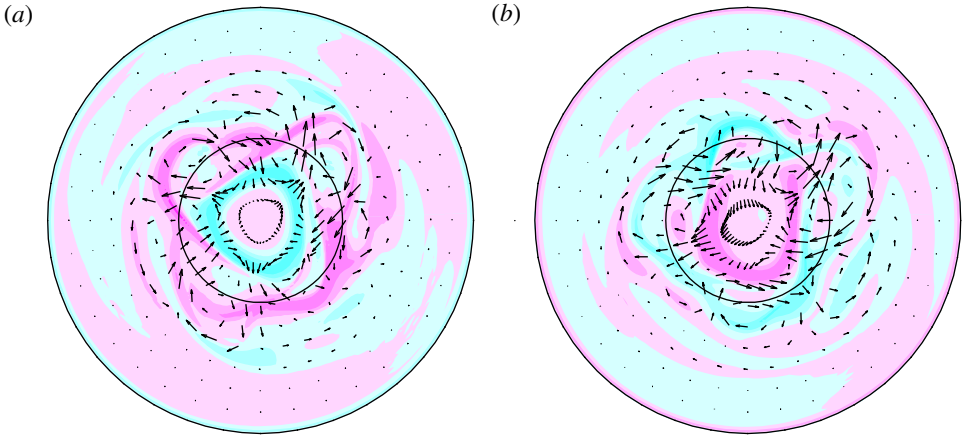


FIGURE 10. Sections of the $10\hat{A}_c$ flow at the levels (*a*) $z = 0.5$ and (*b*) $z = -0.5$. The colours show $\hat{U}_z$, with blue negative, pink positive, and interval 20 ($|\hat{U}_z|_{max} = 107$). The arrows denote the flow ($\hat{U}_s$, $\hat{U}_\phi$) in the plane, but with the axisymmetric part of $\hat{U}_\phi$ (the basic zonal flow) removed to focus on the non-axisymmetric structures. The maximum value of this part of the flow is 104 (compared with a maximum value of ∼700 for the axisymmetric part of $\hat{U}_\phi$, as in the sections in figure 9). The black circles indicate the location of the tangent cylinder.

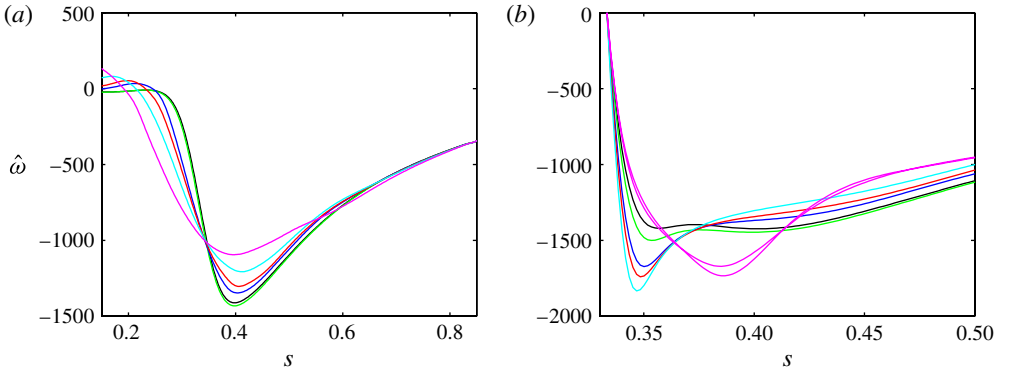


FIGURE 11. Profiles of the axisymmetric angular velocity $\hat{\omega}$ as a function of $s$ along the lines (*a*) $z = 0.5$ and (*b*) $z = 0$. Black denotes $\hat{A} = 0$, green $\hat{A}_c$, blue $2\hat{A}_c$, red $3\hat{A}_c$, cyan $5\hat{A}_c$, and magenta $10\hat{A}_c$. The two magenta curves in (*b*) correspond to two different instants in time; all other curves fluctuate by even smaller amounts (or not at all).

to compare the typical magnitude of the zonal flow, ∼700, with that of all the other flow components, ∼100. The directly forced zonal flow thus still dominates, but the secondary non-axisymmetric structures are not negligible either.

Finally, returning to the entire sequence from $\hat{A} = 0$ to $10\hat{A}_c$, figure 11 quantifies the effect that the increasingly strong three-dimensionality has on the original axisymmetric shear layer. Comparing first the angular velocity profiles at $\hat{A} = 0$ and $\hat{A}_c$, we note that they are almost identical. This demonstrates again the usefulness of the rescaling (2.10), and indicates that, up to the onset of instability at least, the unscaled flow $\boldsymbol{U}$ is exactly proportional to $\hat{A}$. In the supercritical regime we see the gradual broadening of the shear layer previously observed in figure 9. Note also how the peak amplitude in $\hat{\omega}$ decreases monotonically at $z = 0.5$, but at $z = 0$ it increases up to $5\hat{A}_c$, and only decreases again (and shifts noticeably outward) for $10\hat{A}_c$. This reflects the increased $z$-dependence of the zonal flow seen in figure 9.

## 6. Discussion

Having computed these numerical results, we return to the question of whether they could be realized in a liquid-metal (sodium) laboratory experiment, and if so, how much further into the supercritical regime an experiment could be driven. A superconducting magnet with a field strength up to 1 T is currently being built. The spherical device within this magnetic field will have $r_o = 25$ cm, and is intended to rotate up to perhaps 150 revolutions per second.

For comparison, the previous magnetic spherical Couette flow experiments in America (Sisan *et al.* 2004; Kelley *et al.* 2007) and France (Nataf *et al.* 2006, 2008; Brito *et al.* 2011) were comparably sized, but rotated less rapidly. Sisan *et al.* have $r_i = 5$ cm, $r_o = 15$ cm, the inner sphere rotating at up to 50 rev s$^{-1}$, and the outer sphere stationary. Kelley *et al.* have $r_i = 10$ cm, $r_o = 30$ cm and the two spheres rotating independently at up to 45 rev s$^{-1}$ for the inner and 35 rev s$^{-1}$ for the outer. Nataf *et al.* have $r_i = 7.4$ cm, $r_o = 21$ cm, with both spheres rotating independently at up to 30 rev s$^{-1}$. The imposed magnetic field strengths were also somewhat smaller, with an axial field up to 0.2 T for Sisan *et al.*, an axial field up to 0.04 T for Kelley

| | | | | | | | | | | | | |
|---|---|---|---|---|---|---|---|---|---|---|---|---|
| $E$ | $10^{-5}$ | $10^{-6}$ | $10^{-7}$ | $10^{-5}$ | $10^{-6}$ | $10^{-7}$ | $10^{-6}$ | $10^{-7}$ | $10^{-8}$ | $10^{-6}$ | $10^{-7}$ | $10^{-8}$ |
| $\Lambda$ | 1 | 1 | 1 | 1 | 1 | 1 | 3 | 3 | 3 | 6 | 6 | 6 |
| $\hat{A}$ | 3.4 | 1.8 | 1.2 | 34 | 18 | 12 | 100 | 100 | 100 | 300 | 300 | 300 |
| $\Omega/2\pi$ (Hz) | 0.08 | 0.8 | 8.3 | 0.08 | 0.8 | 8.3 | 0.8 | 8.3 | 83 | 0.8 | 8.3 | 83 |
| $B_0$ (T) | 0.01 | 0.03 | 0.10 | 0.01 | 0.03 | 0.10 | 0.06 | 0.18 | 0.56 | 0.08 | 0.25 | 0.80 |
| $I_0$ (A) | 0.33 | 0.55 | 1.2 | 3.3 | 5.5 | 12 | 18 | 55 | 180 | 37 | 120 | 370 |
| $Ro$ | 0.1 | 0.02 | 0.004 | 1 | 0.2 | 0.04 | *1* | *0.3* | *0.1* | *3* | *1* | *0.3* |
| $Rm$ | 0.003 | 0.003 | 0.01 | 0.03 | 0.03 | 0.1 | *0.2* | *0.7* | *2* | *0.7* | *2* | *7* |
| $P$ (W) | $10^{-6}$ | $10^{-5}$ | $10^{-4}$ | $10^{-4}$ | $10^{-3}$ | $10^{-2}$ | *0.02* | *0.6* | *20* | *0.2* | *6* | *200* |

TABLE 2. Each column corresponds to a potential experimental realization, based on a device of size $r_o = 25$ cm. The first three columns correspond to linear onset values from table 1, and the next three to 10 times supercritical. The final six columns illustrate somewhat more extreme parameter values, but which should still be experimentally accessible. The values in italics in these columns are intended to emphasize that these estimates become increasingly unreliable at such strongly supercritical forcing.

*et al.*, and a dipolar field varying between 0.345 and 0.008 T throughout the shell in the French experiment. The $r_o$, $\Omega$ and $B_0$ values intended here are thus ambitious, but still achievable.

The final parameter to consider is the forcing $\hat{A}$. The difficulty lies in estimating how large the currents $I_0$ could reasonably be taken to be. The closest comparable experiment here is probably that of Seilmayer *et al.* (2012), who ran a current of up to 8 kA through a 10 cm diameter column of liquid metal (GaInSn rather than sodium) and studied the resulting Tayler instabilities. We see that very large currents can thus be generated and injected into quite modest-sized volumes of liquid metal. Seilmayer *et al.* also found that even at such extreme currents ohmic heating of the fluid was not excessive, and still allowed run-times of $\sim$20 min before the device warmed up too much and had to be switched off. However, one complication which they did not have to contend with is that here the spherical shell is supposed to be rapidly rotating. The current must therefore either be transferred into the rotating reference frame, or else the entire current-generating apparatus must be included in the rotating frame. Which option would be better is not entirely clear, but it is intended to achieve currents of several hundred amperes.

Table 2 contains some specific numbers, using the liquid sodium values $\rho = 930$ kg m$^{-3}$, $\nu = 6.5 \times 10^{-7}$ m$^2$ s$^{-1}$, $\eta = 8.7 \times 10^{-2}$ m$^2$ s$^{-1}$ and $\mu = 4\pi \times 10^{-7}$ H m$^{-1}$ (e.g. Brito *et al.* 2011). The first three rows indicate the desired non-dimensional input parameters $E$, $\Lambda$ and $\hat{A}$. The next three rows translate these to the corresponding dimensional quantities $\Omega/2\pi$ (that is, converted from rad s$^{-1}$ to rev s$^{-1}$), $B_0$ and $I_0$. We recall that the dimensional and non-dimensional parameters are related by $E = \nu/2\Omega r_o^2$, $\Lambda = B_0^2/2\Omega\mu\rho\eta$ and $\hat{A} = I_0 B_0/4\pi\rho\nu\Omega r_o$, as in (2.13) and (2.14). The next two rows show estimates for the non-dimensional output parameters $Ro$ and $Rm$. $Ro$ has previously been estimated as $Ro \sim 10\hat{A}E^{1/2}$; $Rm$ is estimated below as $Rm \sim Pm\hat{A}E^{-1/2}/3$. The final row shows the estimate (6.3) below for the required power input.

Having demonstrated that even a moderate-sized experiment could be pushed into the strongly supercritical parameter regime $\hat{A} \gg 1$, it is of interest also to return to the original equations, and consider at what point the approximations we made in

deriving (2.11) and (2.12) begin to break down. First, the assumption that $\delta \ll 1$ is easily translated into $Pm\hat{A} \ll \Lambda$, and is thus fulfilled for all plausible parameter values. (Even allowing for the fact that $\boldsymbol{B}_t$ near the shaft would be amplified by a factor of $r_o/r_s$, where $r_s$ is the radius of the shaft, inserting reasonable values for $r_s$ still yields $\boldsymbol{B}_t \ll \boldsymbol{B}_p$.) Furthermore, the induced currents are comparable to the injected currents (figure 7), but not substantially larger, so $\boldsymbol{b} \ll \boldsymbol{B}_p$ is also satisfied.

Next, the neglect of any time-dependence in the induction equation is equivalent to stating that the magnetic Reynolds number $Rm = U_{dim} r_i/\eta$, where $U_{dim}$ is a typical dimensional flow speed, must be small. Recalling our earlier estimate $\hat{U} \sim E^{-1/2}$, and tracing back how $\hat{U}$ scales relative to $U_{dim}$, we obtain $Rm \sim Pm\hat{A}E^{-1/2}/3$. Inserting $Pm = 7.5 \times 10^{-6}$, $\hat{A} = 300$ and $E = 10^{-8}$ yields $Rm \sim 7$, as indicated also in table 2. At the smallest achievable Ekman numbers, and strongest forcings, $Rm$ can therefore exceed $O(1)$, thereby introducing additional dynamics into the problem. For all the solutions numerically computed here though, $Rm$ is indeed small, validating the use of the reduced equations.

Finally, it is of interest to consider the energetics associated with this system, and thereby estimate the power requirements. Taking the dot product of (2.11) with $\hat{\boldsymbol{U}}$, (2.12) with $\Lambda\hat{\boldsymbol{b}}$, adding the two, and integrating over the volume, one obtains the associated energy equation

$$\frac{\partial}{\partial t}\frac{1}{2}E\int |\hat{\boldsymbol{U}}|^2 \,\mathrm{d}V = -\int \hat{U}_\phi f(r,\theta)\,\mathrm{d}V - \int \left(E|\boldsymbol{\nabla}\times\hat{\boldsymbol{U}}|^2 + \Lambda|\boldsymbol{\nabla}\times\hat{\boldsymbol{b}}|^2\right)\mathrm{d}V. \quad (6.1)$$

Recalling that $\hat{U}_\phi$ is negative, the term $-\int \hat{U}_\phi f(r,\theta)\,\mathrm{d}V$ represents the power input, via the work done by the imposed torque $-f(r,\theta)\hat{\boldsymbol{e}}_\phi$. In a statistically steady state this power input is balanced by the viscous and ohmic dissipation, the two negative-definite terms on the right-hand side of (6.1).

Tracing back how the various quantities were non-dimensionalized, the dimensional power input becomes

$$P_{dim} = \frac{I_0 B_0 \nu}{2\pi}\hat{A}\int |\hat{U}_\phi| f \,\mathrm{d}V. \quad (6.2)$$

Using the numerical results to estimate $|\hat{U}_\phi| \sim E^{-1/2}$ (as before), and $\int f\,\mathrm{d}V \sim 2$, one obtains

$$P_{dim} \sim \frac{I_0 B_0 \nu}{\pi}\hat{A}E^{-1/2} = \frac{2\nu^3\rho}{r_o}\hat{A}^2E^{-3/2}. \quad (6.3)$$

As indicated by the last row in table 2, values range from less than one mW to several hundred W at the strongest forcings. That such modest power inputs can nevertheless drive such strong zonal flows demonstrates once again how easily such flows can be maintained once they have been spun up. We caution though that when they are applied so far beyond the linear onset regime, all these formulae for $Ro$, $Rm$ and $P$ are at best very rough order-of-magnitude estimates. Definitive values can only emerge from an actual experiment.

## 7. Conclusion

In this work we have presented a system related to magnetic spherical Couette flow which is driven electromagnetically rather than mechanically, and have demonstrated that an experiment comparable in size to existing Couette flow setups can be driven

strongly enough to yield interesting dynamics, most likely all the way to fully developed turbulence. We suggest furthermore that electromagnetically driven flows of this type offer considerable flexibility in terms of what body forces to impose, far beyond what is possible in Couette flow experiments. To mention just one additional possibility, if the outer electrode were split into multiple segments in the azimuthal direction, so that a non-axisymmetric current pattern could also be imposed, the non-axisymmetric tangent-cylinder shear layers identified by Livermore & Hollerbach (2012) could perhaps be generated. The next step will be the final design of an actual experiment, incorporating as many such options as possible.

## Acknowledgements

This work was supported by ERC grant 247303 (MFECE) to A.J. We thank P. Cardin, S. Fauve, C. Forest, N. Gillet, D. Jault, D. Lathrop, H.-C. Nataf, F. Stefani, and D. Zimmerman for many useful discussions on the technical aspects of liquid metal experiments, and R. Grimmer, P. Scarfe, and Z. Stelzer for ongoing discussions on the details of the planned experiment.

## REFERENCES

BOISSON, J., KLOCHKO, A., DAVIAUD, F., PADILLA, V. & AUMAÎTRE, S. 2012 Travelling waves in a cylindrical magnetohydrodynamically forced flow. *Phys. Fluids* **24**, 044101.

BRITO, D., ALBOUSSIÈRE, T., CARDIN, P., GAGNIÈRE, N., JAULT, D., LA RIZZA, P., MASSON, J.-P., NATAF, H.-C. & SCHMITT, D. 2011 Zonal shear and super-rotation in a magnetized spherical Couette-flow experiment. *Phys. Rev.* E **83**, 066310.

DUCK, P. W. & FOSTER, M. R. 2001 Spin-up of homogeneous and stratified fluids. *Annu. Rev. Fluid Mech.* **33**, 231–263.

EVERETT, J. E. & OSEMEIKHIAN, J. E. 1966 Spherical coils for uniform magnetic fields. *J. Sci. Instrum.* **43**, 470–474.

FIGUEROA, A., DEMIAUX, F., CUEVAS, S. & RAMOS, E. 2009 Electrically driven vortices in a weak dipolar magnetic field in a shallow electrolytic layer. *J. Fluid Mech.* **641**, 245–261.

GISSINGER, C., JI, H. & GOODMAN, J. 2011 Instabilities in magnetized spherical Couette flow. *Phys. Rev.* E **84**, 026308.

HOLLERBACH, R. 1994 Magnetohydrodynamic Ekman and Stewartson layers in a rotating spherical shell. *Proc. R. Soc. Lond.* A **444**, 333–346.

HOLLERBACH, R. 2000 A spectral solution of the magneto-convection equations in spherical geometry. *Intl J. Numer. Meth. Fluids* **32**, 773–797.

HOLLERBACH, R. 2003 Instabilities of the Stewartson layer. Part 1. The dependence on the sign of *Ro*. *J. Fluid Mech.* **492**, 289–302.

HOLLERBACH, R. 2009 Non-axisymmetric instabilities in magnetic spherical Couette flow. *Proc. R. Soc. Lond.* A **465**, 2003–2013.

JONES, C. A. 2011 Planetary magnetic fields and fluid dynamos. *Annu. Rev. Fluid Mech.* **43**, 583–614.

KELLEY, D. H., TRIANA, S. A., ZIMMERMAN, D. S., TILGNER, A. & LATHROP, D. P. 2007 Inertial waves driven by differential rotation in a planetary geometry. *Geophys. Astrophys. Fluid Dyn.* **101**, 469–487.

LATHROP, D. P. & FOREST, C. B. 2011 Magnetic dynamos in the lab. *Phys. Today* **64**, 40–45.

LIVERMORE, P. W. & HOLLERBACH, R. 2012 Successive elimination of shear layers by a hierarchy of constraints in inviscid spherical-shell flows. *J. Math. Phys.* **53**, 073104.

MESSADEK, K. & MOREAU, R. 2002 An experimental investigation of MHD quasi-two-dimensional turbulent shear flows. *J. Fluid Mech.* **456**, 137–159.

MORESCO, P. & ALBOUSSIÈRE, T. 2004 Experimental study of the instability of the Hartmann layer. *J. Fluid Mech.* **504**, 167–181.

NATAF, H.-C., ALBOUSSIÈRE, T., BRITO, D., CARDIN, P., GAGNIÈRE, N., JAULT, D., MASSON, J.-P. & SCHMITT, D. 2006 Experimental study of super-rotation in a magnetostrophic spherical Couette flow. *Geophys. Astrophys. Fluid Dyn.* **100**, 281–298.

NATAF, H. C., ALBOUSSIÈRE, T., BRITO, D., CARDIN, P., GAGNIÈRE, N., JAULT, D. & SCHMITT, D. 2008 Rapidly rotating spherical Couette flow in a dipolar magnetic field: an experimental study of the mean axisymmetric flow. *Phys. Earth Planet. Inter.* **170**, 60–72.

PROUDMAN, I. 1956 The almost-rigid rotation of viscous fluid between concentric spheres. *J. Fluid Mech.* **1**, 505–516.

ROSSI, L., VASSILICOS, J. C. & HARDALUPAS, Y. 2006 Electromagnetically controlled multi-scale flows. *J. Fluid Mech.* **558**, 207–242.

SEILMAYER, M., STEFANI, F., GUNDRUM, T., WEIER, T., GERBETH, G., GELLERT, M. & RÜDIGER, G. 2012 Experimental evidence for a transient Tayler instability in a cylindrical liquid-metal column. *Phys. Rev. Lett.* **108**, 244501.

SISAN, D. R., MUJICA, N., TILLOTSON, W. A., HUANG, Y. M., DORLAND, W., HASSAM, A. B., ANTONSEN, T. M. & LATHROP, D. P. 2004 Experimental observation and characterization of the magnetorotational instability. *Phys. Rev. Lett.* **93**, 114502.

SOWARD, A. M. & DORMY, E. 2010 Shear-layers in magnetohydrodynamic spherical Couette flow with conducting walls. *J. Fluid Mech.* **645**, 145–185.

STEFANI, F., GAILITIS, A. & GERBETH, G. 2008 Magnetohydrodynamic experiments and cosmic magnetic fields. *Z. Angew. Math. Mech.* **88**, 930–954.

STEWARTSON, K. 1966 On almost rigid rotations. Part 2. *J. Fluid Mech.* **26**, 131–144.

VERHILLE, G., PLIHON, N., BOURGOIN, M., ODIER, P. & PINTON, J. F. 2010 Laboratory dynamo experiments. *Space Sci. Rev.* **152**, 543–564.

WEI, X. & HOLLERBACH, R. 2008 Instabilities of Shercliff and Stewartson layers in spherical Couette flow. *Phys. Rev.* E **78**, 026309.